Author/s:
Zhong, QZ;Richardson, JJ;Tian, Y;Tian, H;Cui, J;Mann, S;Caruso, F

Title:
Modular Metal-Quinone Networks with Tunable Architecture and Functionality

Date:
2023-03-27

Citation:
Zhong, Q. Z., Richardson, J. J., Tian, Y., Tian, H., Cui, J., Mann, S. & Caruso, F. (2023). Modular Metal-Quinone Networks with Tunable Architecture and Functionality. Angewandte Chemie International Edition, 62 (14), https://doi.org/10.1002/anie.202218021.

Persistent Link:
https://hdl.handle.net/11343/326474

Nanostructures Hot Paper

How to cite: *Angew. Chem. Int. Ed.* **2023,** *62,* e202218021
International Edition: doi.org/10.1002/anie.202218021
German Edition: doi.org/10.1002/ange.202218021

Modular Metal-Quinone Networks with Tunable Architecture and Functionality

Qi-Zhi Zhong, Joseph J. Richardson, Yuan Tian, Haijiang Tian, Jiwei Cui, Stephen Mann, and Frank Caruso**

Abstract: Nanostructured materials with tunable structures and functionality are of interest in diverse areas. Herein, metal ions are coordinated with quinones through metal-acetylacetone coordination bonds to generate a class of structurally tunable, universally adhesive, hydrophilic, and pH-degradable materials. A library of metal-quinone networks (MQNs) is produced from five model quinone ligands paired with nine metal ions, leading to the assembly of particles, tubes, capsules, and films. Importantly, MQNs show bidirectional pH-responsive disassembly in acidic and alkaline solutions, where the quinone ligands mediate the disassembly kinetics, enabling temporal and spatial control over the release of multiple components using multilayered MQNs. Leveraging this tunable release and the inherent medicinal properties of quinones, MQN prodrugs with a high drug loading (>89 wt %) are engineered using doxorubicin for anti-cancer therapy and shikonin for the inhibition of the main protease in the SARS-CoV-2 virus.

[*] Dr. Q.-Z. Zhong, Prof. F. Caruso
Department of Chemical Engineering, The University of Melbourne
Parkville, Victoria 3010 (Australia)
E-mail: fcaruso@unimelb.edu.au

Dr. Q.-Z. Zhong, Y. Tian, H. Tian, Prof. J. Cui
Key Laboratory of Colloid and Interface Chemistry of the Ministry of Education, School of Chemistry and Chemical Engineering, Shandong University
Jinan, Shandong 250100 (P. R. China)
E-mail: jwcui@sdu.edu.cn

Dr. Q.-Z. Zhong, Prof. S. Mann
Centre for Protolife Research and Centre for Organized Matter Chemistry, School of Chemistry, University of Bristol
Bristol, BS8 1TS (UK)

Dr. J. J. Richardson
School of Engineering, RMIT University
Melbourne, 3000 (Australia)

Introduction

The controlled synthesis of tunable nanomaterials requires the spatial and temporal confinement of components capable of demonstrating diverse interactions with their surrounding environments; this has significant implications for interfacial assembly,[1–3] as well as practical applications in lithography,[4–6] separations,[7] self-cleaning,[8,9] cell adhesion,[10,11] and drug delivery.[12–15] The supramolecular metal-organic toolbox is a promising platform to construct functional materials with tunable properties owing to the rich choice of building blocks and the hybrid physicochemical properties and interactions imparted by the organic and metal components.[16–21] However, the spatial confinement and positioning of specific metal-organic components can be challenging but can be achieved using components that exhibit universal adherence to themselves and to other substrates. To date, this spatial positioning has been achieved, for example using metal-phenolic networks (MPNs),[22–24] where adhesion is derived from the catechol and gallol moieties in the phenolic ligands that can generate different interactions with molecules and substrates. These interactions include hydrogen bonding (e.g., with poly(ethylene glycol), PEG), metal coordination (e.g., with Fe^{3+}), π-π interaction (e.g., with graphene oxide), and hydrophobic interaction (e.g., with aliphatic side chains).[25–30] While the affinity of the catechol moieties to metal ions offers the possibility to tune the disassembly kinetics via the choice of metal ions,[31] the use of different ligands does not significantly change the disassembly kinetics.[32] Therefore, engineering metal-organic materials with high control over disassembly (temporal positioning) while maintaining their versatile adhesion (spatial positioning) characteristics provides a pathway to unlock the potential of tunable metal-organic nanomaterials with inherent functionalities derived from their metal and organic building blocks.

Herein, we present a coordination-driven assembly strategy to engineer functional metal-organic materials with tunable bidirectional pH responsiveness using a library of quinones and metal ions. Quinones are promising natural molecules with particular promise in the medical field. For example, several anticancer drugs containing quinone motifs, e.g., daunomycin, doxorubicin (DOX), mitomycin C, and mitoxantrone, have been approved by the US Food and Drug Administration (FDA) for clinical use. Furthermore, natural quinone compounds, such as cribrostatin, streptonigrin, and β-lapachone, are being studied for their anticancer

activities. Streptonigrin and β-lapachone are already being used as experimental drugs owing to their various pharmacophores and electron transport chains involved in cellular metabolism.[33–35] The quinones were chosen to contain 1,8-naphthoquinone moieties because of: (i) the similar distance between oxygen atoms (0.26 nm) to that of catechol moieties (0.27 nm) for the generation of hydrogen bonding, coordination, and other interactions with substrates and the environment (Figure 1a); (ii) their weaker affinity to metal ions (stability constant for Fe^{3+} is log $K_1 \approx 11$ vs log $K_1 \approx 20$ for catechol moieties)[36,37] that allows the coordination (i.e., metal-acetylacetone) bonds to respond to stimuli (e.g., pH) (Figure 1a); and (iii) their diverse functionalities in biology and electrochemistry owing to their active pharmacophores and electron transport chains.[33–35] Specifically, five quinone ligands (naphthazarin (NZ), shikonin (SK), quinizarin (QZ), anthrarufin (AR), and DOX) and nine metal ions (Al^{3+}, Fe^{2+}, Fe^{3+}, Co^{2+}, Ni^{2+}, Cu^{2+}, Zr^{4+}, Pd^{2+}, and Eu^{3+}) were

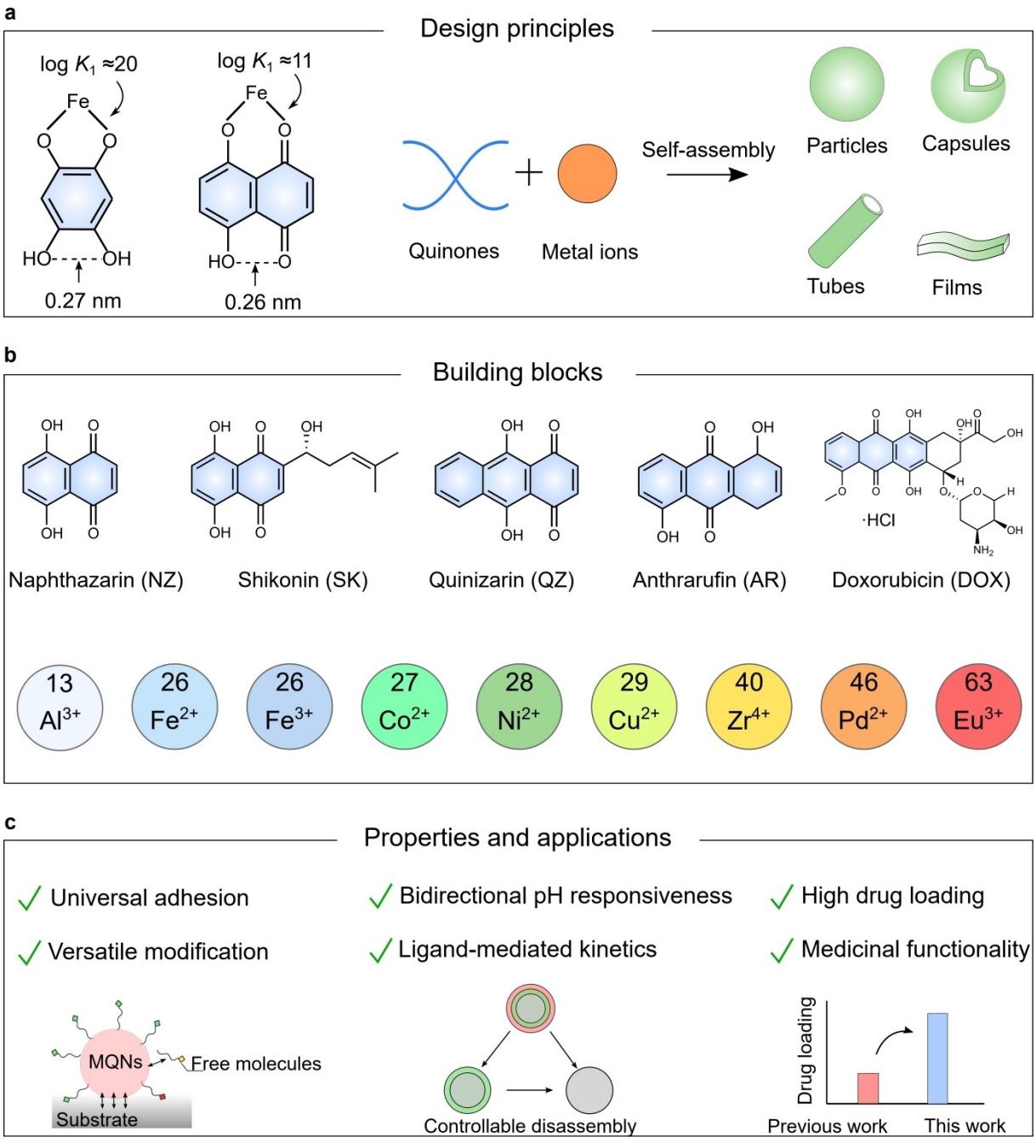

Figure 1. Strategies for the assembly of MQNs with versatile adhesion and controllable disassembly properties. a) Design principles of MQNs, showing the similar distance of adjacent oxygen atoms in catechol and quinone moieties and the different stability constants of Fe^{3+} chelated to catechols and quinones, respectively. b) Library of organic building blocks and metal ions examined in this study to engineer MQNs. c) Properties of MQNs and their potential as prodrugs.

used to create a library of metal-quinone networks (MQNs), including particles, tubes, capsules, and films, in solution and/or on various organic and inorganic substrates (Figure 1a,b). The MQNs were readily post-functionalized with synthetic molecules (e.g., PEG), small natural molecules (e.g., tannic acid (TA) and carboxymethyl chitosan (CCH)), and proteins (e.g., trypsin and catalase). Importantly, the MQNs showed bidirectional pH responsiveness, enabling their disassembly in both acidic and alkaline solutions with ligand-mediated kinetics. This subsequently allowed for the controllable release of cargo in a one-step or stepwise process (Figure 1c). Considering the medicinal functionality of quinones, prodrugs comprising DOX (an approved anthracycline drug) or SK (a clinically trialed drug candidate) were synthesized with a high drug loading (>89 wt %) for the inhibition of tumor cell growth and the main protease (M^{pro}) in coronaviruses, respectively. Our study provides a paradigm for engineering tunable, universally adherent metal-organic architectures with spatially confined components, allowing for their controlled temporal disassembly into functional molecules. These engineered materials are expected to find specific applications in drug delivery, separation membranes,[38] soft actuators,[39] and synthetic life.[40]

Results and Discussion

Assembly of MQNs

We first describe the formation of MQNs between Fe^{3+} and the relatively simple quinone ligand NZ. The NZ solution transitioned from red to purple-black within 30 s after the addition of an aqueous solution of Fe^{3+} (Figure S1). UV/Vis spectroscopy analysis revealed a new absorbance peak around 650 nm in the spectrum of the Fe^{3+}-NZ suspension, which indicated coordination bond formation (Figure S1).[41,42] Hollow Fe^{3+}-NZ tubes were observed by transmission electron microscopy (TEM, Figure 2a) and scanning electron microscopy (SEM, Figure S2) after 2 h of incubation, whereas a longer incubation time (e.g., 48 h) led to the formation of monodisperse nanoparticles (Figure 2b). This transformation is likely caused by the etching of the needle-like NZ crystals by free Fe^{3+},[43,44] leading to needle-like tubes, followed by further etching into small aggregates (< 5 nm) of coordination complexes that subsequently assemble and grow into particles (Figure S3). SEM images and dynamic light scattering analysis revealed the uniform size ($\approx$220 nm in diameter) and the polydispersity index (0.05) of the Fe^{3+}-NZ particles (Figure 2b, Figure S4). In addition, Fe^{3+}-NZ networks could form conformal films on polystyrene (PS) particles (Figure S5), shifting the ζ-potential of the PS particles from −24 to 31 mV after coating. After removal of the PS templates, Fe^{3+}-NZ capsules with a single-wall thickness of $\approx$89 nm were obtained (Figure 2c, Figure S6), demonstrating the robust and interconnected nature of the chelation networks. The Young's modulus of the Fe^{3+}-NZ capsules was estimated to be $\approx$1.3 GPa by atomic force microscopy (AFM) measurements (Figure S7), which is similar to that of Fe^{3+}-TA films ($\approx$1.0 GPa).[22] Fe^{3+}-NZ films deposited on quartz slides had a thickness of $\approx$7.2 nm and a root-mean-square roughness of $\approx$5.8 nm, as measured by AFM (Figure 2d).

To evaluate the modularity of the assembly route, a number of quinone ligands (i.e., NZ, SK, QZ, AR, and DOX) and various metal ions (Al^{3+}, Fe^{3+}, Fe^{2+}, Co^{2+}, Ni^{2+}, Cu^{2+}, Zr^{4+}, Pd^{2+}, and Eu^{3+}) were used to synthesize particles. These ligands were chosen for their different sizes and structures, while the metals were chosen at random, suggesting that a much wider array of ligands and metals should be applicable to this approach. Incubation of SK, QZ, AR, or DOX with Fe^{3+} for 8 h resulted in the formation of particles with diameters of 173 ± 15, 131 ± 10, 128 ± 9, and 251 ± 15 nm (Figure 2e–h, Figure S8), respectively. The combination of NZ and QZ with the other metal ions was also examined and all resulted in the formation of particles in bulk solution (Figure 2i–l and Figure S8) and coatings on polyester fibers (Figure 2m). All metal ion solutions changed color after the addition of NZ, and all resulting mixed solutions featured new absorbance peaks in their UV/Vis spectra (Figure S9, Figure S1), suggesting coordination.[45,46] Energy-dispersive X-ray spectroscopy (EDS) analysis indicated the homogeneous distribution of the selected metal ions in the coatings (Figure 2m). These results highlight that template-assisted MQN coatings and capsules, as well as template-free MQN tubes and particles can readily be synthesized from different quinone and metal ion building blocks.

Chemistry and Chelation of MQNs

As observed from the powder X-ray diffraction (PXRD) pattern in Figure 3a, the Fe^{3+}-NZ films displayed a broad amorphous hump at 20° with crystalline peaks, suggesting that the MQNs can co-exist as amorphous and crystalline states.[47] UV/Vis spectroscopy revealed that the absorbance peak of the Fe^{3+}-NZ films was around 650 nm (Figure 3b), indicating that the MQNs had identical coordination bonds to the Fe^{3+}-NZ networks in suspension. X-ray photoelectron spectroscopy (XPS) revealed that the dominant oxidation state of iron in the films was Fe^{3+}, as deduced from the presence of Fe $2p_{3/2}$ peaks at 712 eV with a 2p peak separation of $\approx$14 eV (Figure S10).[7] Further analysis of the O 1s spectra indicated the presence of Fe–O bonds at 530.4 eV and Fe–OH bonds at 533.2 eV in the Fe^{3+}-NZ networks (Figure 3c).[40] Raman spectroscopy confirmed the vibration of Fe–O in the networks owing to the bands observed in the low-frequency regions of 550–650 and 380–420 cm^{-1} (Figure S11).[47] In addition, Fourier transform infrared spectroscopy (FTIR) showed a shift in C=O absorbance from 1621 to 1532 cm^{-1} (Figure 3d), indicating the chelation of C=O to Fe^{3+}.[48] The increase in transmittance at $\approx$3450 cm^{-1} observed in the spectrum of the Fe^{3+}-NZ powders, relative to the transmittance of pure NZ powders, can be attributed to the stretching of O–H in the networks, suggesting the chelation of water/hydroxyl in the complexes.[49] Furthermore, high-resolution mass spectrome-

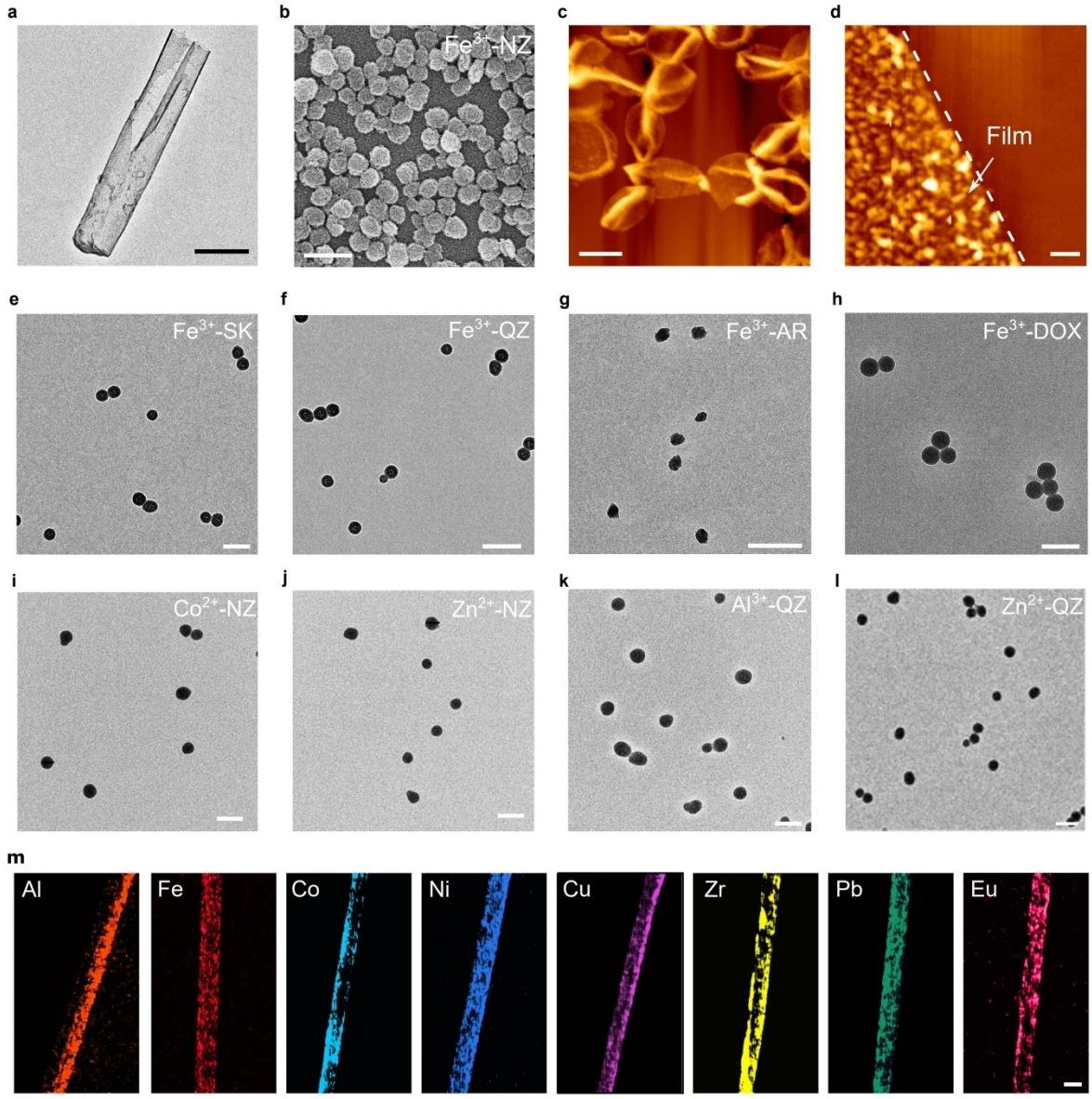

Figure 2. Synthesis of MQNs with various building blocks. a) TEM image of an Fe^{3+}-NZ tube (obtained after incubation for 2 h), scale bar is 500 nm. b) SEM image of Fe^{3+}-NZ particles (obtained after prolonged incubation for 48 h), scale bar is 300 nm. c) AFM image of Fe^{3+}-NZ capsules, scale bar is 3 μm. d) AFM image of a scratched Fe^{3+}-NZ film on a quartz slide, scale bar is 1 μm. e)–h) TEM images of MQN particles prepared with Fe^{3+} and various quinones, scale bars are 400 nm. i)–l) TEM images of MQN particles prepared with NZ or QZ and different metal ions (incubation time 8 h), scale bars are 2 μm (i,j,l) and 500 nm (k). m) EDS images of MQN coatings on polyester fibers prepared with NZ and various metal ions; the scale bar is 50 μm.

try analysis of Fe^{3+}-NZ dispersions revealed the presence of mono-, bis-, and tris-type Fe^{3+}-NZ complexes in the networks (Figure S12), demonstrating that amorphous structures are dominant in the MQNs (a phenomenon that is more common for amorphous metal-organic materials such as MPNs).

The MQNs display a range of chelation possibilities owing to the 1,8-naphthoquinone moieties that can provide binding sites to chelate multinuclear Fe^{3+} species by forming Fe–O and Fe–C=O bonds (Figure 3e). NZ molecules can act as bidentate ligands to generate mono-, bis-, and tri-type complexes with Fe^{3+} (Figure S12). These multidentate complexes provide bridges to form the coordination networks. In addition to NZ, water molecules and/or hydroxyls can chelate to Fe^{3+} to form polymeric Fe species (e.g., μ-oxo/hydroxo species) due to the hydrolysis of Fe^{3+} in aqueous solutions. In contrast to the small number of polymeric Fe species in MPNs, which are generally too few to detect experimentally,[47] the presence of μ-oxo/hydroxo species in MQNs may contribute to the responsiveness of the metal-quinone coordination bonds owing to their access to the surrounding solvent.[18] It is worth noting that other interactions, such as hydrogen bonding and π-π interaction, could also contribute to the formation of MQNs.

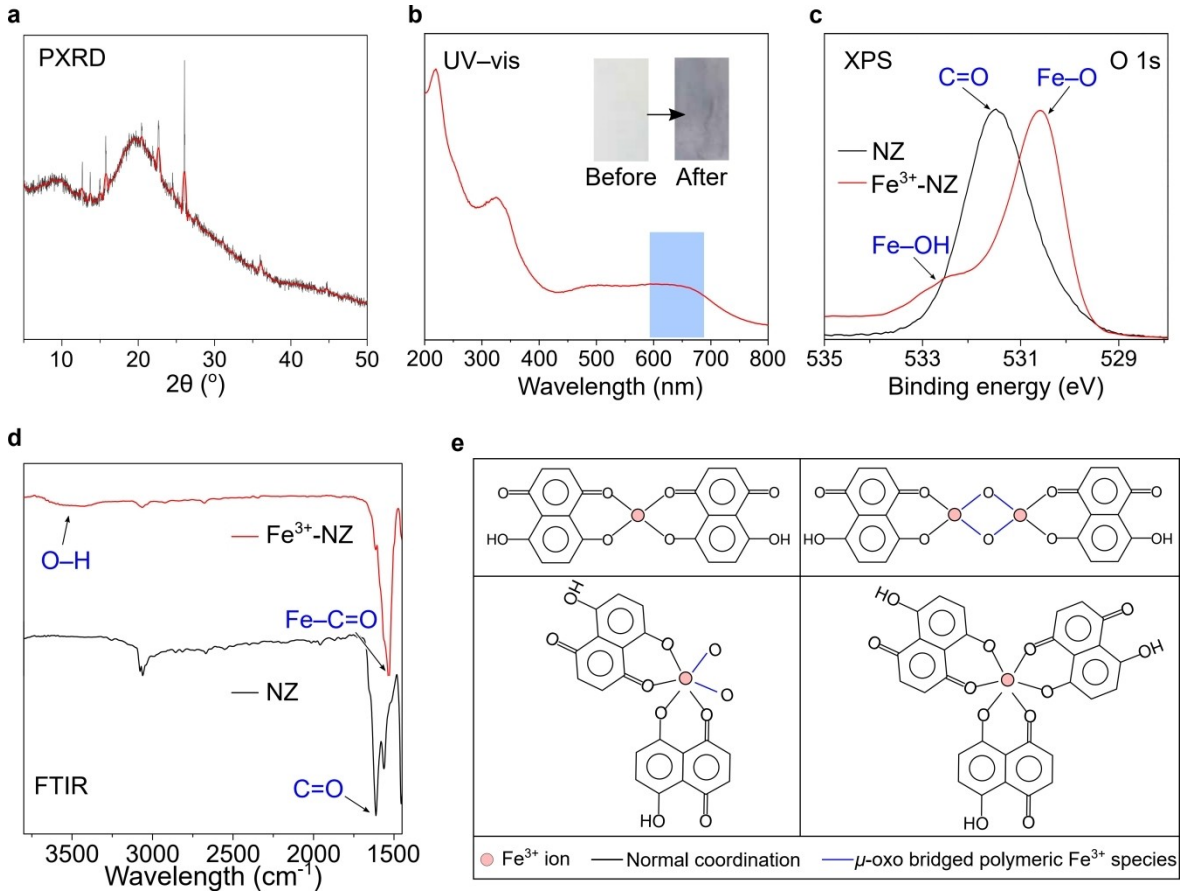

Figure 3. Characterization and structures of MQNs. a) PXRD spectrum of Fe^{3+}-NZ capsules. The black and red lines represent the raw and smoothed data, respectively. b) UV/Vis absorption spectrum of Fe^{3+}-NZ films, insets are photographs of quartz slides before and after coating. c) XPS spectra of NZ and Fe^{3+}-NZ networks showing the presence of Fe–O and Fe–OH bonds in the networks. d) FTIR spectra of NZ and Fe^{3+}-NZ powders showing the presence of Fe–O=C and O–H bonds in the networks. e) Proposed schematic representation of the possible coordination structures of MQNs.

Versatile Adhesion of MQNs

To evaluate the ability of MQN films to coat different surfaces, Fe^{3+}-NZ networks were used to coat a range of substrates with different sizes, shapes, and compositions, including polymers (polytetrafluoroethylene (PTFE), poly(methyl methacrylate) (PMMA), PS, polycarbonate (PC), polyvinyl chloride (PVC), and acrylonitrile butadiene styrene resin (ABS)), noble metals (Au), metal plates with a native oxide surface (stainless steel (SS), Cu/CuO, Al/Al_2O_3, Ti/TiO_2), and minerals (Si/SiO_2 and quartz). After coating, all studied substrates turned purple-black, suggesting successful deposition of MQN films. The water contact angles of the planar substrates changed to $<30°$ (Figure 4a, b), indicating the formation of hydrophilic coatings on the substrate surface. The low water contact angle can be attributed to both the increased roughness from the micro- and nanoscale structures and the hydrophilic nature of the metal ions (Figure S13) in the films.[50] SiO_2 particles with diameters of $\approx$1.3 μm could also be coated with Fe^{3+}-NZ films (Figure S14). The diverse interactions (e.g., hydrogen bonding, π-π interaction, and cation-π interaction) that enable deposition on different substrates are primarily derived from the quinones.[51] For example, the distance between the oxygen atoms of 1,8-naphthoquinone moieties (0.26 nm) is reported to enable coordination interactions with metal ions and hydrogen bonds with minerals (e.g., mica with a distance of adjacent O atoms of 0.28 nm)[52] (see the discussion in the caption of Figure S15).

In addition to enabling deposition on surfaces, the versatile adhesion of Fe^{3+}-NZ networks allows for the conjugation of various functional molecules to MQNs (Figure 4c). For example, amino-containing molecules (e.g., 4-arm NH_2-PEG) could couple covalently with quinone molecules through Michael addition and Schiff base reactions to form a PEGylated layer on the surface of Fe^{3+}-NZ particles (Figure 4d and Figure S16).[51] These PEGylated layers endowed the Fe^{3+}-NZ particles with good dispersibility and colloidal stability in aqueous solutions (Figure 4e and Figure S17). Besides synthetic molecules, small naturally occurring molecules could readily be conjugated to Fe^{3+}-NZ, including TA, phytic acid (PA), and CCH, which shifted the ζ-potential of the Fe^{3+}-NZ particles to approximately −35, −19, and −11 mV, respectively (Figure 4f). In addition, Fe^{3+}-NZ particles can adsorb a range of proteins on their surface. For example, a trypsin corona with a layer

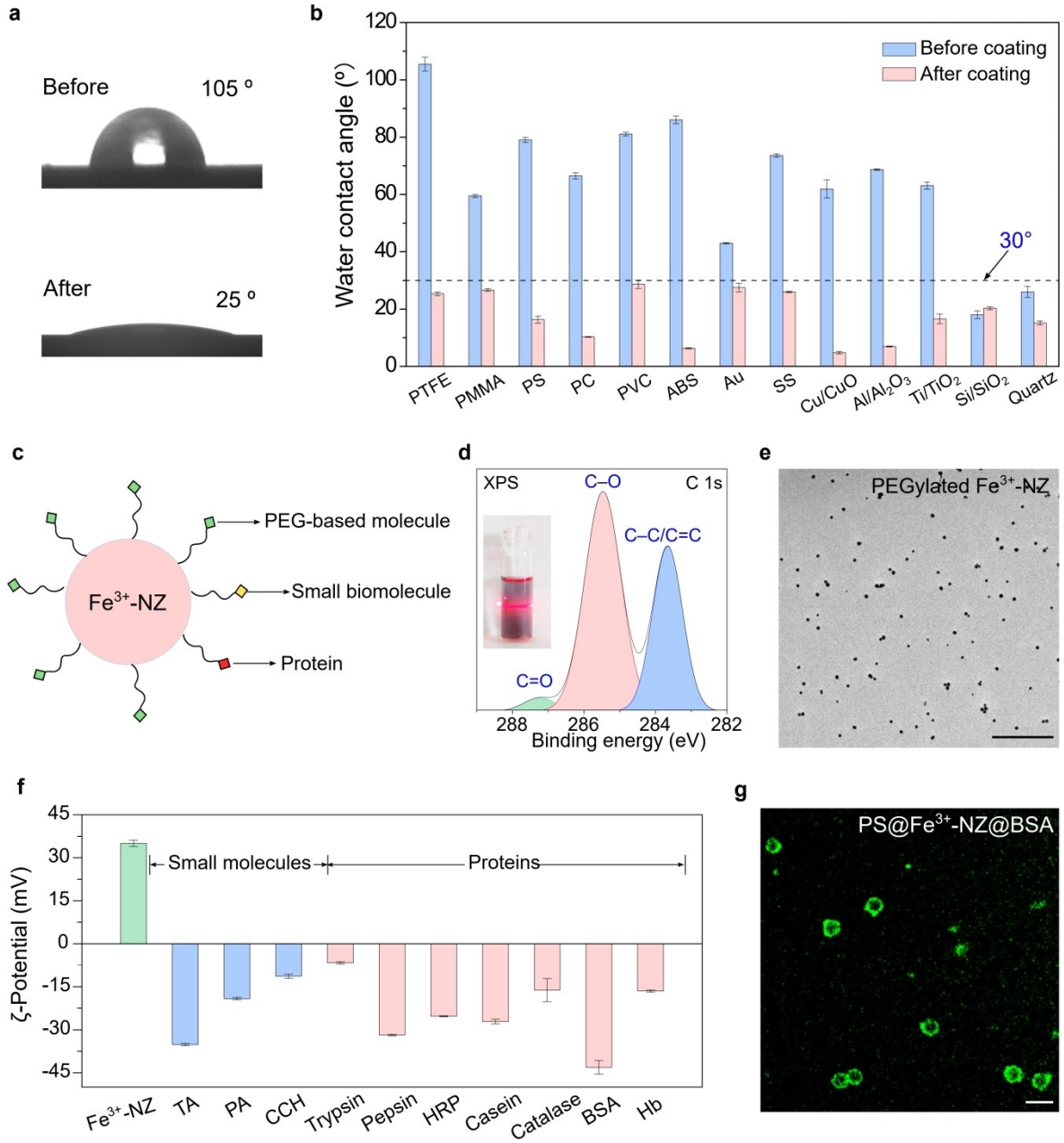

Figure 4. Formation of MQN films on various substrates and their modification with functional molecules. a) Photographs of a PTFE surface showing the water contact angle before and after Fe^{3+}-NZ coating. b) Water contact angles of different planar substrates before and after Fe^{3+}-NZ coating. c) Schematic illustration of the modification of MQN particles with functional molecules. d) XPS spectra of Fe^{3+}-NZ particles modified with NH_2-PEG; inset is a photograph of the particle suspension showing the Tyndall effect. e) TEM image of NH_2-PEG-modified Fe^{3+}-NZ particles; the scale bar is 4 μm. f) ζ-Potential values of Fe^{3+}-NZ particles coated with different molecules and proteins (TA, PA, CCH, trypsin, pepsin, horseradish peroxidase (HRP), casein, catalase, BSA, and hemoglobin (Hb)). g) CLSM image of PS@Fe^{3+}-NZ@BSA particles (BSA labeled with FITC); the scale bar is 4 μm.

thickness ranging from 17 to 42 nm could be deposited on Fe^{3+}-NZ particles (Figure S18). Bovine serum albumin (BSA, labeled with fluorescein isothiocyanate (FITC)) could also coat the surface of Fe^{3+}-NZ particles, yielding green fluorescent rings when viewed by confocal laser scanning microscopy (CLSM) (Figure 4g). The presence of these protein layers altered the ζ-potential of the Fe^{3+}-NZ particles mainly depending on the isoelectric points of the proteins and their interactions with MQNs (Figure 4f).[53] This water-based adsorption process did not impede the catalytic activity of the particles, as catalase-coated NZ particles could decompose H_2O_2 to H_2O and O_2 (Figure S19). The pristine Fe^{3+}-NZ particles without catalase did not produce oxygen bubbles (data not shown).

Controllable Disassembly of MQNs and Functional Molecule Release

To demonstrate the dynamic nature of metal-quinone coordination bonds, Fe^{3+}-NZ networks were studied at various pH. The color of the Fe^{3+}-NZ network suspension was dependent on pH: i.e., pink at $pH \leq 2$, purple-black at $3 \leq pH \leq 9$, and blue at $pH \geq 10$ (Figure 5a). In contrast, NZ solutions were red within the pH range of $3 \leq pH \leq 8$ (Figure S20), suggesting the important role of the NZ–Fe ion interactions within this pH range. UV/Vis spectroscopy of the Fe^{3+}-NZ networks in suspension further showed the occurrence of the characteristic absorbance band at ≈650 nm, of which the absorbance increased as the pH increased from 2 to 9 (Figure 5b), confirming the coordinated state of the networks. In contrast, the UV/Vis spectra of the Fe^{3+}-NZ suspension and NZ solution appeared comparable at pH values below 2 and above 9 (Figure S21), indicating that free NZ molecules are predominant (vs Fe^{3+}-NZ network) at these pH values. The weaker presence of Fe^{3+}-NZ networks is likely because of the destabilization of the coordination bonds occurring at low pH (e.g., $pH < 2$) owing to the protonation of the hydroxyl groups (Figure 5c).[22] At high pH (e.g., $pH > 9$), disassembly and precipitation of Fe complexes occur upon hydrolysis of Fe^{3+} because of the low stability constant and the μ-oxo bridged polymeric Fe species,[41] resulting in the characteristic absorbance of quinones at ≈620 nm and ≈570 nm. As for Fe^{3+}-NZ films, only ≈10 % of the films disassembled after 120 h of incubation at pH 7.8, whereas ≈30 % and 60 % of the films dissembled at pH 5.0 and pH 3.0, respectively (Figure 5d, Figure S22). The films completely disassembled within 5 min at pH 1.2 (Figure 5d). At higher pH values, ≈50 % of the films disassembled after 120 h at pH 10.0, and the films completely disassembled within 3 min at pH 13.3.

This bidirectional pH-responsive disassembly feature opens up the possibility to engineer asymmetric responses to environmental stimuli. In particular, tuning the pH response is an essential feature in applications such as drug delivery. While metals have been shown to control the disassembly of MPNs to some extent, ligands offer increased possibilities owing to the richer choice of molecules available and therefore would be more valuable for controlling disassembly kinetics. To study the release of the ligands from MQNs, we first chose pH 5.0 to match the acidic environment of the endosomal and lysosomal compartments. We found that at pH 5.0, nearly 100 % of DOX was released from Fe^{3+}-DOX particles, whereas only ≈52 %, 35 %, 20 %, and 4 % of NZ, AR, QZ, and SK were disassembled from their respective MQN particles (Figure 5e, Figure S23). Additional chelation sites (e.g., SK), π-π interactions (e.g., anthraquinone moieties in AR and QZ), and ionic interactions (e.g., DOX) likely influence the stability of MQN particles and therefore allow for disassembly and ligand release in a tunable way. For example, Fe^{3+}-SK and Fe^{3+}-SK@Fe^{3+}-NZ coatings were deposited on PS particles (denoted as PS@Fe^{3+}-SK and PS@Fe^{3+}-SK@Fe^{3+}-NZ, respectively); the resulting black particles displayed ζ-potentials of 14 and 31 mV, respectively (Figure 5f). After incubation at pH 3.0 for 24 h, the supernatant was pink-orange due to the release of NZ, whereas the pellets (e.g., PS@Fe^{3+}-SK particles) remained black with a ζ-potential of ≈15 mV (similar to that of the as-prepared PS@Fe^{3+}-SK particles). Further incubation at pH 2.0 for 24 h did not significantly change the color of the supernatant or the ζ-potential of the particles, which suggests that the Fe^{3+}-NZ network coatings were completely disassembled, whereas the Fe^{3+}-SK coatings remained intact at pH 2.0. Nevertheless, incubation at pH 1.2 for 24 h caused the Fe^{3+}-SK coatings to disassemble, leading to pristine white PS particles, reverting to their original ζ-potential (−25 mV), and red SK in the supernatant. In addition to the stepwise release achieved at lower pH values, a single burst release could be triggered at higher pH values. Specifically, incubation at pH 13.3 led to the rapid and complete disassembly of both Fe^{3+}-NZ and Fe^{3+}-SK coatings in one step within 10 min of incubation. These results demonstrate the bidirectional pH-dependent and ligand-mediated disassembly of MQNs, highlighting that functional molecules can be released with temporal and spatial control.

MQN Prodrugs for Cancer Therapy and Inhibition of Viral M^{pro}

The MQN particles can be used therapeutically without the need for any cargo. For example, DOX, an FDA-approved anthracycline drug that is widely used to treat numerous types of cancer,[54,55] was used to fabricate Fe^{3+}-DOX nanoparticles. The drug (DOX) loading was ≈93.8 wt % (Figure 6a), which represents a considerably higher drug weight percentage than the FDA-approved liposomal formulation of DOX, Doxil™ (≈11 wt % of DOX). The in vitro cytotoxicity of the Fe^{3+}-DOX particles was evaluated on HeLa cells and murine mammary carcinoma cells (4T1 cells). The Fe^{3+}-DOX particles exhibited a concentration-dependent cytotoxicity against both cancer cell lines (Figure 6b, Figure S24). After incubation for 48 h, the Fe^{3+}-DOX particles showed a similar cytotoxicity to that of free DOX.

MQN prodrugs are also promising for targeting other diseases such as the inhibition of M^{pro} of SARS-CoV-2. M^{pro} is a key enzyme of coronaviruses and plays a pivotal role in mediating viral replication and transcription, making it an attractive drug target for SARS-CoV-2 and similar viruses (Figure 6c).[56] Recently, SK, an active ingredient in traditional Chinese and Japanese herbs as well as a clinically trialed drug candidate for inflammation[57] has been shown to inhibit M^{pro}.[58] The inhibition of M^{pro} by Fe^{3+}-SK capsules (diameter of ≈3.5 μm and a thickness of ≈76 nm, Figure 6d) was then examined and monitored over time and at different concentrations. At 1 mg mL^{-1} Fe^{3+}-SK capsules, ≈91 % of M^{pro} was inhibited after 4 h of incubation, whereas at 0.5 mg mL^{-1} Fe^{3+}-SK capsules, only ≈50 % of M^{pro} was inhibited (Figure 6e, Figure S25), indicating the controllable release of SK for inhibiting M^{pro}.

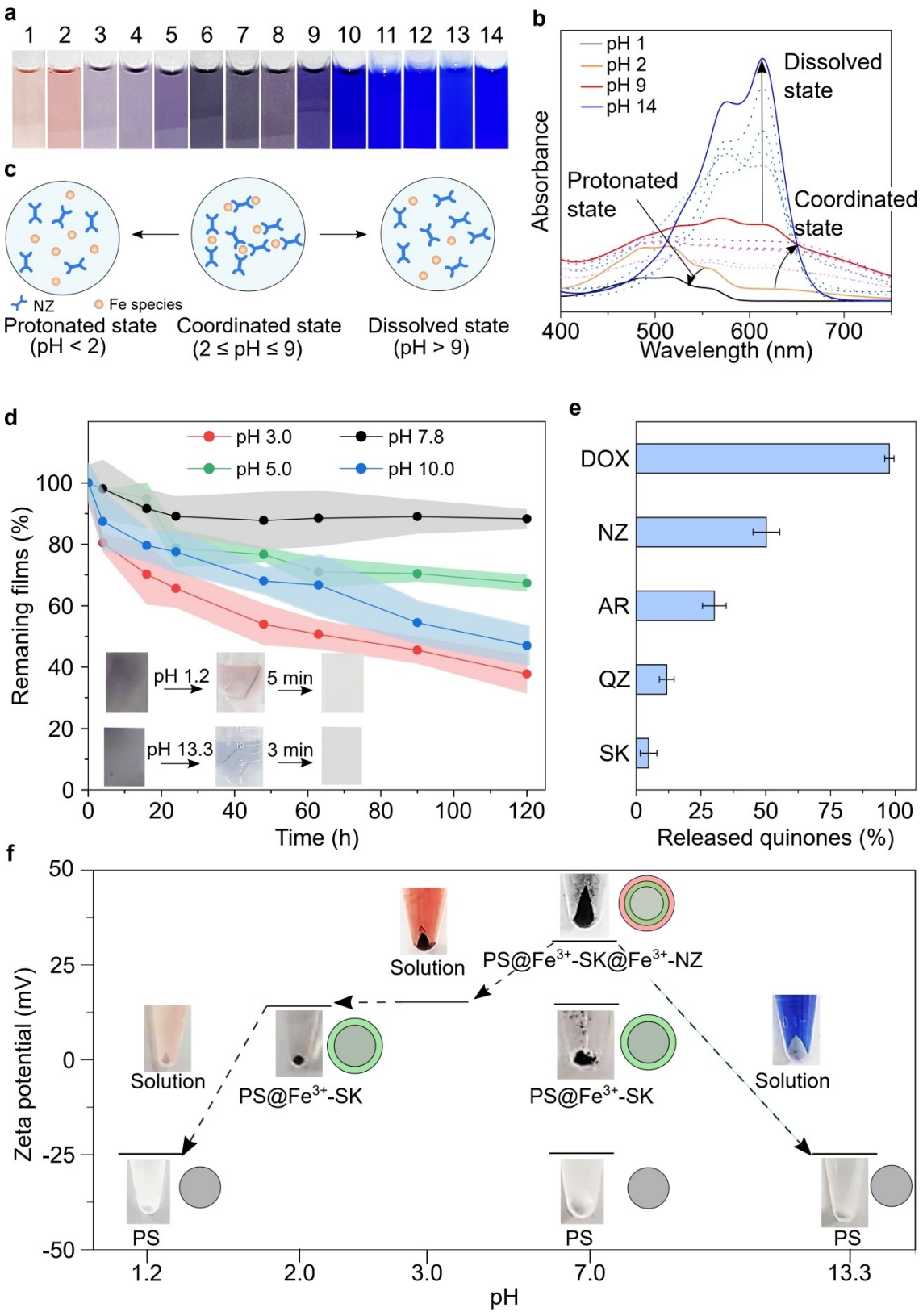

Figure 5. Bidirectional pH responsiveness and ligand-mediated disassembly of MQNs. a) MQN suspensions and b) their corresponding UV/Vis absorption spectra at different pH values. c) Schematic representation of MQN states at different pH values. d) Plot of the remaining films as a function of time; insets are images of MQN films on quartz slides before (left) and after (right) immersion in pH 1.2 or pH 13.3 solution (middle). Shaded areas represent standard deviations of triplicates, with the mean represented by the data point. e) Percentage of quinones released from MQN particles after incubation at pH 5.0 for 8 h. f) ζ-Potential of the particles before and after disassembly; insets are images showing the washed pellets or pellets with supernatant containing released quinones after 24 h at pH 3.0, 2.0, and 1.2, and after 10 min at pH 13.3.

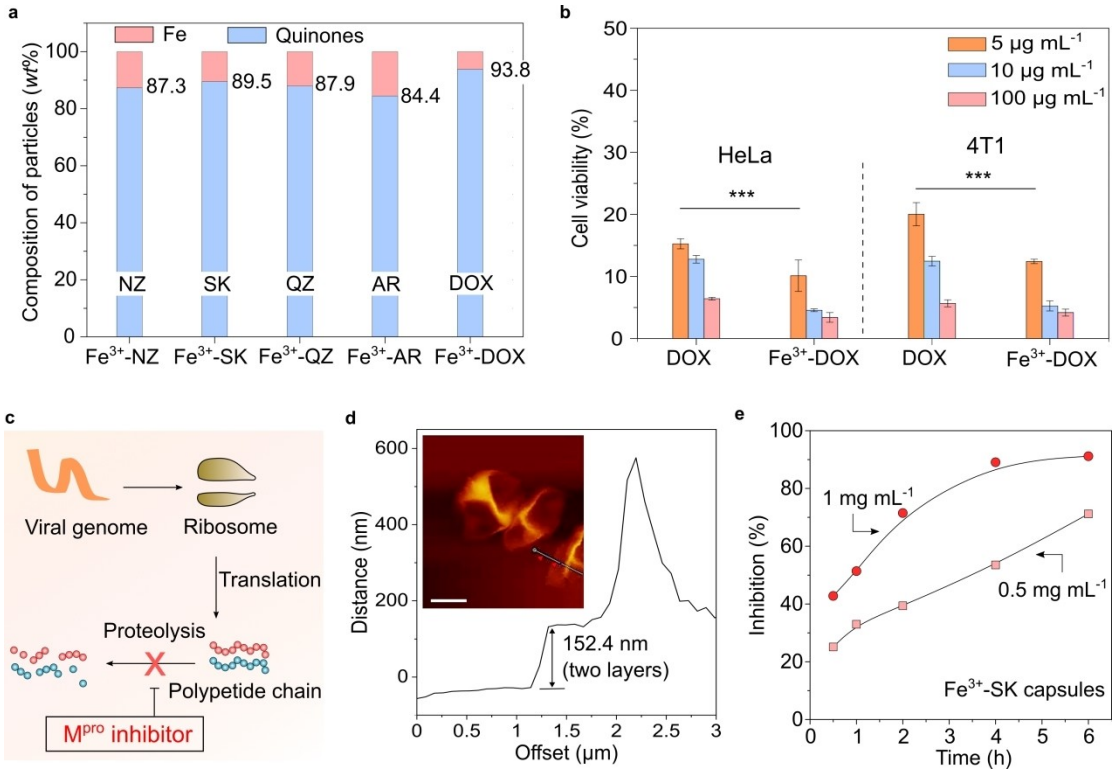

Figure 6. Application of MQNs as prodrugs. a) Composition of different MQN particles. b) Viability of HeLa and 4T1 cells after incubation with free DOX or Fe^{3+}-DOX particles for 48 h (mean ± standard deviation, $n=5$), *** indicates $p<0.01$ (one-way analysis of variance (ANOVA) test). c) Proposed infection mechanism of SARS-CoV-2 as a model virus containing M^{pro}. d) AFM image of Fe^{3+}-SK capsules (inset) and their corresponding height profile; the scale bar is 2 μm. e) Inhibition rate of M^{pro} using Fe^{3+}-SK capsules at different capsule concentrations and times.

Conclusion

We have demonstrated a coordination-driven strategy to engineer metal-organic tubes, particles, capsules, and films with universal adhesion and tunable disassembly properties. The diverse interfacial interactions of quinones allow MQNs to be engineered as hydrophilic coatings on a wide range of substrates, as well as reactive platforms for functionalization with molecules capable of fluorescence, enzymatic catalysis, and increased colloidal stability. An important feature of MQNs is that they display bidirectional pH responsiveness (disassembly at $pH<2$ and $pH>10$) and ligand-mediated disassembly features, which collectively allow for the controllable release of multiple components in a single step or in a stepwise manner. Moreover, as quinones are functional molecules in themselves, Fe^{3+}-DOX particles and Fe^{3+}-SK capsules can be engineered as prodrugs for cancer therapy and M^{pro} inhibition. We anticipate that the present study will open up avenues for generating complex and tunable stimuli-responsive metal-organic films and particles for various applications.

Supporting Information

Supporting Information is available from the Wiley Online Library or from the author.

Acknowledgements

This research was conducted and funded by the Australian Research Council (ARC) through the Discovery Project (DP200100713) Scheme. J.C. acknowledges funding support from the National Natural Science Foundation of China (22072075, 21872085). The authors acknowledge Dr. René Lafleur at The University of Melbourne for assistance with the molecular structure calculations, Dr. Jingqu Chen at The University of Melbourne for assistance with the cell viability assay, Qian Wang at Shandong University for assistance with the inductively coupled plasma measurements, and Mengqi Li at Shandong University for assistance with the atomic force microscopy measurements. Open Access publishing facilitated by The University of Melbourne, as part of the Wiley - The University of Melbourne agreement via the Council of Australian University Librarians.

Conflict of Interest

The authors declare no conflict of interest.

Data Availability Statement

The data that support the findings of this study are available from the corresponding author upon reasonable request.

Keywords: Metal-Organic Particles · Nanostructures · Prodrugs · Quinones · Self-Assembly

[1] J. J. Richardson, M. Björnmalm, F. Caruso, *Science* **2015**, *348*, aaa2491.
[2] H. Lee, S. M. Dellatore, W. M. Miller, P. B. Messersmith, *Science* **2007**, *318*, 426.
[3] X. Hou, Y. Hu, A. Grinthal, M. Khan, J. Aizenberg, *Nature* **2015**, *519*, 70.
[4] J. Cai, C. Li, N. Kong, Y. Lu, G. Lin, X. Wang, Y. Yao, I. Manners, H. Qiu, *Science* **2019**, *366*, 1095.
[5] D. Y. Ryu, K. Shin, E. Drockenmuller, C. J. Hawker, T. P. Russell, *Science* **2005**, *308*, 236.
[6] J. C. Love, L. A. Estroff, J. K. Kriebel, R. G. Nuzzo, G. M. Whitesides, *Chem. Rev.* **2005**, *105*, 1103.
[7] Q.-Z. Zhong, S. Li, J. Qu, K. Xie, S. Pan, J. J. Richardson, F. Caruso, *Angew. Chem. Int. Ed.* **2019**, *58*, 12563; *Angew. Chem.* **2019**, *131*, 12693.
[8] B. Su, Y. Tian, L. Jiang, *J. Am. Chem. Soc.* **2016**, *138*, 1727.
[9] A. Gao, Q. Wu, D. Wang, Y. Ha, Z. Jun, P. Yang, *Adv. Mater.* **2016**, *28*, 579.
[10] J. Li, A. D. Celiz, J. Yang, Q. Yang, I. Wamala, W. Whyte, B. R. Seo, N. V. Vasilyev, J. J. Vlassak, Z. Suo, D. J. Mooney, *Science* **2017**, *357*, 378.
[11] J. Huang, S. Liu, C. Zhang, X. Wang, J. Pu, F. Ba, S. Xue, H. Ye, T. Zhao, K. Li, Y. Wang, J. Zhang, L. Wang, C. Fan, T. K. Lu, C. Zhong, *Nat. Chem. Biol.* **2019**, *15*, 34.
[12] Z. Tang, X. Zhang, Y. Shu, M. Guo, H. Zhang, W. Tao, *Nano Today* **2021**, *36*, 101019.
[13] Y. Yang, B. Sun, S. Zuo, X. Li, S. Zhou, L. Li, C. Luo, H. Liu, M. Cheng, Y. Wang, S. Wang, Z. He, J. Sun, *Sci. Adv.* **2020**, *6*, eabc1725.
[14] J. Yu, J. Wang, Y. Zhang, G. Chen, W. Mao, Y. Ye, A. R. Kahkoska, J. B. Buse, R. Langer, Z. Gu, *Nat. Biomed. Eng.* **2020**, *4*, 499.
[15] W. Ngo, B. Stordy, J. Lazarovits, E. K. Raja, C. L. Etienne, W. C. W. Chan, *J. Am. Chem. Soc.* **2020**, *142*, 17938.
[16] A. Bétard, R. A. Fischer, *Chem. Rev.* **2012**, *112*, 1055.
[17] L. Li, G. Zhang, Z. Su, *Angew. Chem. Int. Ed.* **2016**, *55*, 9093; *Angew. Chem.* **2016**, *128*, 9239.
[18] E. Khare, N. Holten-Andersen, M. J. Buehler, *Nat. Rev. Mater.* **2021**, *6*, 421.
[19] E. Degtyar, M. J. Harrington, Y. Politi, P. Fratzl, *Angew. Chem. Int. Ed.* **2014**, *53*, 12026; *Angew. Chem.* **2014**, *126*, 12220.
[20] L. Heinke, C. Wöll, *Adv. Mater.* **2019**, *31*, 1806324.
[21] P. Falcaro, K. Okada, T. Hara, K. Ikigaki, Y. Tokudome, A. W. Thornton, A. J. Hill, T. Williams, C. Doonan, M. Takahashi, *Nat. Mater.* **2017**, *16*, 342.
[22] H. Ejima, J. J. Richardson, K. Liang, J. P. Best, M. P. van Koeverden, G. K. Such, J. Cui, F. Caruso, *Science* **2013**, *341*, 154.
[23] J. Guo, B. L. Tardy, A. J. Christofferson, Y. Dai, J. J. Richardson, W. Zhu, M. Hu, Y. Ju, J. Cui, R. R. Dagastine, I. Yarovsky, F. Caruso, *Nat. Nanotechnol.* **2016**, *11*, 1105.
[24] M. A. Rahim, S. L. Kristufek, S. Pan, J. J. Richardson, F. Caruso, *Angew. Chem. Int. Ed.* **2019**, *58*, 1904; *Angew. Chem.* **2019**, *131*, 1920.
[25] Q.-Z. Zhong, J. J. Richardson, S. Li, W. Zhang, Y. Ju, J. Li, S. Pan, J. Chen, F. Caruso, *Angew. Chem. Int. Ed.* **2020**, *59*, 1711; *Angew. Chem.* **2020**, *132*, 1728.
[26] J. Zhou, Z. Lin, Y. Ju, M. A. Rahim, J. J. Richardson, F. Caruso, *Acc. Chem. Res.* **2020**, *53*, 1269.
[27] S. Ma, C. Yan, M. Cai, X. Wang, F. Zhou, W. Liu, *Adv. Mater.* **2018**, *30*, 1803371.
[28] Q. Zhao, D. W. Lee, B. K. Ahn, S. Seo, Y. Kaufman, J. N. Israelachvili, J. H. Waite, *Nat. Mater.* **2016**, *15*, 407.
[29] G. P. Maier, M. V. Rapp, J. H. Waite, J. N. Israelachvili, A. Butler, *Science* **2015**, *349*, 628.
[30] C. Lim, J. Huang, S. Kim, H. Lee, H. Zeng, D. S. Hwang, *Angew. Chem. Int. Ed.* **2016**, *55*, 3342; *Angew. Chem.* **2016**, *128*, 3403.
[31] J. Guo, Y. Ping, H. Ejima, K. Alt, M. Meissner, J. J. Richardson, Y. Yan, K. Peter, D. von Elverfeldt, C. E. Hagemeyer, F. Caruso, *Angew. Chem. Int. Ed.* **2014**, *53*, 5546; *Angew. Chem.* **2014**, *126*, 5652.
[32] R. Liu, J. Zhao, Q. Han, X. Hu, D. Wang, X. Zhang, P. Yang, *Adv. Mater.* **2018**, *30*, 1802851.
[33] M. Ninomiya, Y. Ando, F. Kudo, K. Ohmori, K. Suzuki, *Angew. Chem. Int. Ed.* **2019**, *58*, 4264; *Angew. Chem.* **2019**, *131*, 4308.
[34] L. F. Tietze, H. P. Bell, S. Chandrasekhar, *Angew. Chem. Int. Ed.* **2003**, *42*, 3996; *Angew. Chem.* **2003**, *115*, 4128.
[35] H. Wang, P. Hu, J. Yang, G. Gong, L. Guo, X. Chen, *Adv. Mater.* **2015**, *27*, 2348.
[36] H. Lee, W. Il Kim, W. Youn, T. Park, S. Lee, T.-S. Kim, J. F. Mano, I. S. Choi, *Adv. Mater.* **2018**, *30*, 1805091.
[37] M. D. Engelmann, R. Hutcheson, I. F. Cheng, *J. Agric. Food Chem.* **2005**, *53*, 2953.
[38] D. V. Andreeva, M. Trushin, A. Nikitina, M. C. F. Costa, P. V. Cherepanov, M. Holwill, S. Chen, K. Yang, S. W. Chee, U. Mirsaidov, A. H. C. Neto, K. S. Novoselov, *Nat. Nanotechnol.* **2021**, *16*, 174.
[39] J. Huang, Y. Liu, Y. Yang, Z. Zhou, J. Mao, T. Wu, J. Liu, Q. Cai, C. Peng, Y. Xu, B. Zeng, W. Luo, G. Chen, C. Yuan, L. Dai, *Sci. Robot.* **2021**, *6*, eabe1858.
[40] N. Martin, L. Tian, D. Spencer, A. Coutable-Pennarun, J. L. R. Anderson, S. Mann, *Angew. Chem. Int. Ed.* **2019**, *58*, 14594; *Angew. Chem.* **2019**, *131*, 14736.
[41] H. Yu, Q.-Z. Zhong, T. G. Liu, W. Z. Qiu, B. H. Wu, Z. K. Xu, L. S. Wan, *Langmuir* **2019**, *35*, 3643.
[42] R. Chaisuksant, W. Palkawong-na-ayuthaya, K. Grudpan, *Talanta* **2000**, *53*, 579.
[43] L. Guo, A. Wang, P. Hu, A. Tian, R. Hao, D. Yu, J. Yang, D. Chen, H. Wang, *RSC Adv.* **2018**, *8*, 2077.
[44] H. Wang, W. Zhu, Y. Ping, C. Wang, N. Gao, X. Yin, C. Gu, D. Ding, C. J. Brinker, G. Li, *ACS Appl. Mater. Interfaces* **2017**, *9*, 14258.
[45] L. Tabrizi, M. Fooladivanda, H. Chiniforoshan, *BioMetals* **2016**, *29*, 981.
[46] R. S. Bottei, P. L. Gerace, *Inorg. Nucl. Chem. Lett.* **1961**, *23*, 245.
[47] M. A. Rahim, K. Kempe, M. Müllner, H. Ejima, Y. Ju, M. P. van Koeverden, T. Suma, J. A. Braunger, M. G. Leeming, B. F. Abrahams, F. Caruso, *Chem. Mater.* **2015**, *27*, 5825.
[48] R. Siebner-Freibach, S. Yariv, Y. Lapides, Y. Hadar, Y. Chem, *J. Agric. Food Chem.* **2005**, *53*, 3434.
[49] Q.-Z. Zhong, S. Pan, M. A. Rahim, G. Yun, J. Li, Y. Ju, Z. Lin, Y. Han, Y. Ma, J. J. Richardson, F. Caruso, *ACS Appl. Mater. Interfaces* **2018**, *10*, 33721.
[50] Q.-Z. Zhong, M. H. Yi, Y. Du, A. He, Z. K. Xu, L. S. Wan, *Adv. Mater. Interfaces* **2017**, *4*, 1700490.
[51] Q.-Z. Zhong, J. J. Richardson, A. He, T. Zheng, R. P. M. Lafleur, J. Li, W.-Z. Qiu, D. Furtado, S. Pan, Z.-K. Xu, L.-S. Wan, F. Caruso, *Angew. Chem. Int. Ed.* **2021**, *60*, 2346; *Angew. Chem.* **2021**, *133*, 2376.
[52] Q. Ye, F. Zhou, W. Liu, *Chem. Soc. Rev.* **2011**, *40*, 4244.
[53] C. Liu, T. Wan, H. Wang, S. Zhang, Y. Ping, Y. Cheng, *Sci. Adv.* **2019**, *5*, eaaw8922.
[54] K. Liang, J. E. Chung, S. J. Gao, N. Yongvongsoontorn, M. Kurisawa, *Adv. Mater.* **2018**, *30*, 1706963.
[55] Y. Dai, Z. Yang, S. Cheng, Z. Wang, R. Zhang, G. Zhu, Z. Wang, B. C. Yung, R. Tian, O. Jacobson, C. Xu, Q. Ni, J. Song, X. Sun, G. Niu, X. Chen, *Adv. Mater.* **2018**, *30*, 1704877.

[56] H. F. Florindo, R. Kleiner, D. Vaskovich-Koubi, R. C. Acúrcio, B. Carreira, E. Yeini, G. Tiram, Y. Liubomirski, R. Satchi-Fainaro, *Nat. Nanotechnol.* **2020**, *15*, 630.
[57] V. P. Papageorgiou, A. N. Assimopoulou, E. A. Couladouros, *Angew. Chem. Int. Ed.* **1999**, *38*, 270; *Angew. Chem.* **1999**, *111*, 280.
[58] Z. Jin, X. Du, Y. Xu, Y. Deng, M. Liu, Y. Zhao, B. Zhang, X. Li, L. Zhang, C. Peng, Y. Duan, J. Yu, L. Wang, K. Yang, F. Liu, R. Jiang, X. Yang, T. You, X. Liu, X. Yang, F. Bai, H. Liu, X. Liu, L. W. Guddat, W. Xu, G. Xiao, C. Qin, Z. Shi, H. Jiang, Z. Rao, H. Yang, *Nature* **2020**, *582*, 289.

Manuscript received: December 7, 2022
Accepted manuscript online: February 2, 2023
Version of record online: February 20, 2023